Electron-ion heating partition in imbalanced solar-wind turbulence

Jonathan Squire,[1] Romain Meyrand,[1] and Matthew W. Kunz[2, 3]

[1]*Physics Department, University of Otago, Dunedin 9010, New Zealand*
[2]*Department of Astrophysical Sciences, Princeton University, Peyton Hall, Princeton, NJ 08544, USA*
[3]*Princeton Plasma Physics Laboratory, PO Box 451, Princeton, NJ 08543, USA*

ABSTRACT

A likely candidate mechanism to heat the solar corona and solar wind is low-frequency "Alfvénic" turbulence sourced by magnetic fluctuations near the solar surface. Depending on its properties, such turbulence can heat different species via different mechanisms, and the comparison of theoretical predictions to observed temperatures, wind speeds, anisotropies, and their variation with heliocentric radius provides a sensitive test of this physics. Here we explore the importance of normalized cross helicity, or imbalance, for controlling solar-wind heating, since it a key parameter of magnetized turbulence and varies systematically with wind speed and radius. Based on a hybrid-kinetic simulation in which the forcing's imbalance decreases with time—a crude model for a plasma parcel entrained in the outflowing wind—we demonstrate how significant changes to the turbulence and heating result from the "helicity barrier" effect. Its dissolution at low imbalance causes its characteristic features—strong perpendicular ion heating with a steep "transition-range" drop in electromagnetic fluctuation spectra—to disappear, driving more energy into electrons and parallel ion heat, and halting the emission of ion-scale waves. These predictions seem to agree with a diverse array of solar-wind observations, offering to explain a variety of complex correlations and features within a single theoretical framework.

1. INTRODUCTION

The solar corona and its extended outflow, the solar wind, provide us with an unparalleled laboratory for studying the physics of magnetized collisionless plasmas. Decades of observations have revealed a highly complex system filled with fluctuations across a vast range of scales, with properties that can be correlated in surprising and nontrivial ways with the plasma's flow speed, temperatures, anisotropies, and elemental abundances (Marsch 2006; Horbury et al. 2012; Bruno & Carbone 2013). These correlations, as well as the extended heating at large heliocentric distances needed to explain the high speed of fast-wind streams (Parker 1965), suggest that the solar wind is shaped by both properties of its low-coronal source and turbulent heating at larger altitudes. Of particular interest are the decades of observations that hint at the role played by the fluctuations' *imbalance* (i.e., normalized cross helicity), a key parameter in the theory of magnetized turbulence (Dobrowolny et al. 1980; Schekochihin 2022) that is observed to correlate with wind speed U and decrease with increasing

heliocentric radius R (e.g., Roberts et al. 1987; Marsch 2006; D'Amicis et al. 2021; Shi et al. 2023).

In this Letter, we argue for the importance of imbalance in shaping turbulence and heating in the low-β solar wind. We focus on the physics of the "helicity barrier" (Meyrand et al. 2021), a constraint in $\beta \ll 1$ plasmas that prevents the imbalanced fraction of the turbulent energy from cascading from large scales to below the ion gyroradius ρ_i, thus "trapping" much of the energy at scales above ρ_i. This strongly curtails electron heating and causes the turbulence to grow to large amplitudes, eventually enabling perpendicular ion heating. The resulting fluctuation spectra and ion velocity distribution function (VDF; f_i) match features measured in the low-β solar wind well (Squire et al. 2022; hereafter S+22), particularly the properties of the steep "transition range" drop in electromagnetic field spectra around ρ_i scales (e.g., Duan et al. 2021; Bowen et al. 2022, 2023).

Our results here are based on a simulation of forced Alfvénic turbulence in which the imbalance is slowly decreased in time, capturing the transition between the highly imbalanced and balanced regimes. This setup serves two purposes: first, it is a crude model for the expected response of the turbulent heating as the plasma flies outwards from the Sun and its imbalance naturally decreases; second, it tests the robustness of helicity-

jonathan.squire@otago.ac.nz

barrier physics in the face of complex ion-kinetic physics and lower imbalance (where its effects are weaker). We observe slowly increasing electron heating in good agreement with simple predictions, while the ion heating rapidly switches off when the forcing becomes balanced and the system is no longer constrained by the helicity barrier. The mechanism naturally explains the observed correlation of wind speed with ion temperatures, as well as the switch from negative to positive correlation of wind speed with electron temperature at increasing R (e.g., Burlaga & Ogilvie 1973; Marsch et al. 1989; Shi et al. 2023). Correlations with other properties such as the spectral transition range, proton VDFs, and plasma-wave/instability activity seem to explain a diverse array of observations within a single theoretical framework.

2. NUMERICAL METHOD AND SETUP

We use the hybrid-kinetic method implemented in the `Pegasus++` code (Kunz et al. 2014; Arzamasskiy et al. 2023). This approach treats the ion (proton) dynamics fully kinetically using a particle-in-cell (PIC) approach, while the electrons constitute a massless, neutralizing, isothermal fluid. The ion macro-particle positions ($\boldsymbol{r}$) and velocities ($\boldsymbol{v}$) are drawn from an initially Maxwellian $f_i(\boldsymbol{v})$ and evolved via

$$\frac{\mathrm{d}\boldsymbol{r}}{\mathrm{d}t} = \boldsymbol{v}, \quad \frac{\mathrm{d}\boldsymbol{v}}{\mathrm{d}t} = \frac{e}{m_i}\left[\boldsymbol{E}(\boldsymbol{r},t) + \frac{\boldsymbol{v}}{c}\times\boldsymbol{B}(\boldsymbol{r},t)\right] + \frac{1}{m_i}\boldsymbol{F}_\perp^U,$$
(1)

where $\boldsymbol{E}$ and $\boldsymbol{B}$ are the electric and magnetic fields and $\boldsymbol{F}_\perp^U$ stirs turbulence by injecting incompressible motions perpendicular ("$\perp$") to a mean ("guide") magnetic field $\boldsymbol{B}_0$. The magnetic field satisfies a modified version of Faraday's law,

$$\frac{\partial\boldsymbol{B}}{\partial t} = -c\boldsymbol{\nabla}\times(\boldsymbol{E}+\boldsymbol{F}_\perp^B) + \eta_4\nabla^4\boldsymbol{B},$$
(2)

where $\boldsymbol{F}_\perp^B$ forces solenoidal magnetic fluctuations perpendicular to $\boldsymbol{B}_0$ and η_4 is a hyper-resistivity that absorbs small-scale magnetic energy. The electric field is

$$\boldsymbol{E} = -\frac{\boldsymbol{u}}{c}\times\boldsymbol{B} - \frac{T_e}{en}\boldsymbol{\nabla}n + \frac{(\boldsymbol{\nabla}\times\boldsymbol{B})\times\boldsymbol{B}}{4\pi en},$$
(3)

where n is the ion (and electron) density and $\boldsymbol{u}$ is the ion flow velocity, both of which are computed via a weighted sum of the marker particles in the relevant region of space; T_e is the electron temperature, which is a parameter of the model; and e, m_i, and c are the electron/ion charge, the ion mass, and the speed of light, respectively. We also define the Alfvén speed $v_\mathrm{A} \equiv B_0/\sqrt{4\pi n m_i}$, the ion gyrofrequency $\Omega_i \equiv eB_0/(m_i c)$, and the "Elsässer" fields $\boldsymbol{z}^\pm \equiv \boldsymbol{u}_\perp \pm \boldsymbol{B}_\perp/\sqrt{4\pi n m_i} \equiv \boldsymbol{u}_\perp \pm \boldsymbol{b}_\perp$. Volume averages are denoted by $\langle\cdot\rangle$ and $f_i(w_\perp, w_\parallel)$ is the gyro-averaged VDF, with $w_\perp$ and $w_\parallel$ the particle velocities perpendicular and parallel to the local magnetic field in the frame of the plasma (i.e., $\boldsymbol{w} \equiv \boldsymbol{v} - \boldsymbol{u}$).

Our basic simulation set up follows S+22. The simulation represents a small co-moving patch of plasma, capturing realistic solar-wind turbulence amplitudes and anisotropies around $k_\perp\rho_i \sim 1$ scales. The domain is Cartesian and periodic, with coordinates $\{x,y,z\}$, and is elongated along $\boldsymbol{B}_0 = -B_0\hat{\boldsymbol{z}}$, with $L_z = 6L_\perp$ and $L_\perp = 67.5d_i$, where $d_i = v_\mathrm{A}/\Omega_i$ is the ion inertial length. With these parameters, the box shape approximately matches the (statistical) shape of turbulent eddies measured at similar scales in the solar wind (Chen et al. 2016; S+22). The grid resolution is $N_\perp^2 \times N_z = 392^2 \times 2352$, so that the smallest resolved scales are $k_{\perp,\mathrm{max}}d_i \simeq \pi N_\perp d_i/L_\perp \approx 18$. We use $N_\mathrm{ppc} = 216$ ion-macroparticles per cell. The hyper-resistivity was increased from $\eta_4 \approx 2.4\times10^{-5}d_i^4\Omega_i$ to $\eta_4 = 5\times10^{-5}d_i^4\Omega_i$ midway through the simulation in response to the strengthening kinetic-range cascade.

The simulation is initialized at $t = 0$ using the final snapshot from S+22, and thus represents saturated highly imbalanced turbulence with strong perpendicular ion heating and a helicity barrier, similar to turbulence observed in the near-Sun solar wind by PSP (Bowen et al. 2023). The initial ion temperature is such that $\beta_i = 8\pi\langle nT_i\rangle/\langle B^2\rangle \approx 0.33$; electrons are isothermal with $\beta_{e0} = 8\pi\langle n\rangle T_e/B_0^2 = 0.3$. The simulation is run for an additional $\approx 18\tau_\mathrm{A}$, where $\tau_\mathrm{A} = L_z/v_\mathrm{A}$ is the outer-scale Alfvén time, which is also comparable to the turnover time of the turbulence $\tau_\mathrm{turb} \sim L_\perp/u_\mathrm{rms}$ due to our choice of forcing parameters (see below; $u_\mathrm{rms} = \langle u^2\rangle^{1/2}$ is the root-mean-square velocity). Because the ions heat up, β_i increases over the course of the simulation to $\simeq 0.45$ and $\rho_i = \sqrt{\beta_i}d_i$ changes modestly. The domain resolves scales between $k_{\perp 0}\rho_{i0} \equiv 2\pi\rho_{i0}/L_\perp \approx 0.05$ and $k_{\perp\mathrm{max}}\rho_{i0} \approx 10$, where $\rho_{i0} = \rho_i(t=0)$.

2.1. Decreasing imbalance with distance from the Sun

A novel feature of this work is the forcing, which changes from imbalanced to balanced over the simulation, heuristically mimicking the radial evolution of the solar wind. Noting that the energy density $\langle|\boldsymbol{z}^+|^2 + |\boldsymbol{z}^-|^2\rangle/4$ and cross-helicity density $\langle|\boldsymbol{z}^+|^2 - |\boldsymbol{z}^-|^2\rangle/4$ are each invariants of the reduced (or incompressible) MHD equations (i.e., for $k_\perp\rho_i \ll 1$ Alfvénic fluctuations, ignoring density variation), we define the injection rates of energy and cross helicity as ε and ε_H, respectively. We also define the injection rates of Elsässer energies $\varepsilon^\pm \equiv (\varepsilon \pm \varepsilon_H)/2$. The forcing functions $\boldsymbol{F}_\perp^U$ and $\boldsymbol{F}_\perp^B$ are intended to capture the effect of stirring due to turbulent eddies above the box scale, consisting of random combinations of large-scale Fourier modes with wavenumbers k_j satisfying $2\pi/L_j \leq k_j \leq 4\pi/L_j$ for $j = \{x,y,z\}$. They are computed as $\boldsymbol{F}_\perp^U = f^U\boldsymbol{F}_0$ and $\boldsymbol{\nabla}\times\boldsymbol{F}_\perp^B = f^B\boldsymbol{F}_0$, where $\boldsymbol{F}_0$ is divergence-free, perpendicular to $\boldsymbol{B}_0$, and evolved in time via an Ornstein–Uhlenbeck process with correlation time $\tau_\mathrm{A}/2$. We fix ε and ε_H at each time step by adjusting f^U and f^B so that $n\boldsymbol{u}\cdot\boldsymbol{F}_\perp^U$ and $\boldsymbol{B}\cdot\boldsymbol{\nabla}\times\boldsymbol{F}_\perp^B$ take the values needed to

inject the required energies into $\boldsymbol{z}^{\pm}$. $\boldsymbol{F}_{\perp}^{B}$ is computed from $\boldsymbol{F}_0$ via a fast Fourier transform and used in the standard `Pegasus++` constrained-transport algorithm to evolve $\boldsymbol{B}$, ensuring that $\boldsymbol{\nabla} \cdot \boldsymbol{B} = 0$ to machine precision.

We fix $\varepsilon = C_{\mathrm{A}} m_i n (L_{\perp}/L_z)^2 v_{\mathrm{A}}^2 V / \tau_{\mathrm{A}} \approx 37 m_i n v_{\mathrm{A}}^2 \Omega_i d_i^3$, where $C_{\mathrm{A}} = 0.29$ is the Kolmogorov constant and V is the simulation volume; the factor $(L_{\perp}/L_z)^2 v_{\mathrm{A}}^2 / \tau_{\mathrm{A}}$ guarantees critically balanced fluctuations at the outer scale with $u_{\mathrm{rms}} \sim (L_{\perp}/L_z) v_{\mathrm{A}}$ and $\tau_{\mathrm{turb}} \sim \tau_{\mathrm{A}}$. In contrast, ε_H decreases in time during the simulation so that the "injection imbalance" $\varepsilon_H/\varepsilon$ starts at 0.9 (as in S+22) then decreases linearly in time at a rate of 0.1 every $1.5\tau_{\mathrm{A}}$, reaching $\varepsilon_H = 0$ (balanced forcing) at $t = 13.5\tau_{\mathrm{A}}$, where it remains for the rest of the simulation (see Fig. 1). Because the cross helicity and energy are approximately conserved at $k_{\perp}\rho_i \ll 1$ scales, this evolution is intended to mimic crudely the effect of larger scales becoming more balanced with radius, thereby driving the smaller scales with decreasing $\varepsilon_H/\varepsilon$. However, in the actual solar wind, the timescale over which the imbalance decreases is comparable to both the turbulent decay timescale and the expansion timescale $\tau_{\mathrm{exp}} \approx R/U$ (Meyrand et al. 2023). By keeping ε fixed, we effectively assume that the turbulent decay and expansion are slow compared to the simulation's duration, which is appropriate since $\tau_{\mathrm{exp}}/\tau_{\mathrm{A}} \simeq 1300\,(B/80\,\mathrm{nT})(R/35\,\mathrm{R_{\odot}})(U/350\,\mathrm{km\,s^{-1}})^{-1}$. However, this also implies that our adopted imbalance-decrease timescale of $\approx 15\tau_{\mathrm{A}}$ is much too short. This trade-off is unavoidable given the extreme computational expense of kinetic-turbulence simulations, but it should be kept mind that the simulation can only qualitatively capture realistic features of this transition in the solar wind.

3. RESULTS

The properties of the saturated imbalanced turbulence, from which the system is initialized, are discussed in S+22. Due to the helicity barrier, only the balanced fraction of the injected energy flux, $\simeq 2\varepsilon^-$, can cascade to scales below $k_{\perp}\rho_i \sim 1$. In reality, this flux would heat electrons, but in the hybrid simulation it is absorbed by the hyper-resistive dissipation ε_{η}, which indeed is measured to be $\varepsilon_{\eta} \simeq 2\varepsilon^-$. Fluctuations reach large amplitudes and (through critical balance) small parallel scales approaching $k_{\parallel}d_i \sim 1$, where they become oblique ion-cyclotron waves (ICWs) with frequencies $\omega(\boldsymbol{k})$ that approach Ω_i (Li et al. 1999). Such ICWs strongly scatter "resonant" particles with $w_{\parallel} = w_{\parallel \mathrm{res}} \equiv \omega(\boldsymbol{k})/k_{\parallel} - \Omega_i/k_{\parallel}$ (Kennel & Engelmann 1966), causing quasi-linear heating that absorbs the remaining energy input once there is sufficient power in modes with $w_{\parallel \mathrm{res}} \sim v_{\mathrm{th}}$.

The basic evolution as the injection imbalance decreases is shown in Fig. 1; a portion of the saturated phase of the simulation from S+22 is shown at $t < 0$ for comparison. The imbalance of the fluctuations,

$$\sigma_c \equiv \frac{\langle |\boldsymbol{z}^+|^2 \rangle - \langle |\boldsymbol{z}^-|^2 \rangle}{\langle |\boldsymbol{z}^+|^2 \rangle + \langle |\boldsymbol{z}^-|^2 \rangle} = \frac{2\langle \boldsymbol{u}_{\perp} \cdot \boldsymbol{b}_{\perp} \rangle}{\langle |\boldsymbol{u}_{\perp}|^2 \rangle + \langle |\boldsymbol{b}_{\perp}|^2 \rangle}, \quad (4)$$
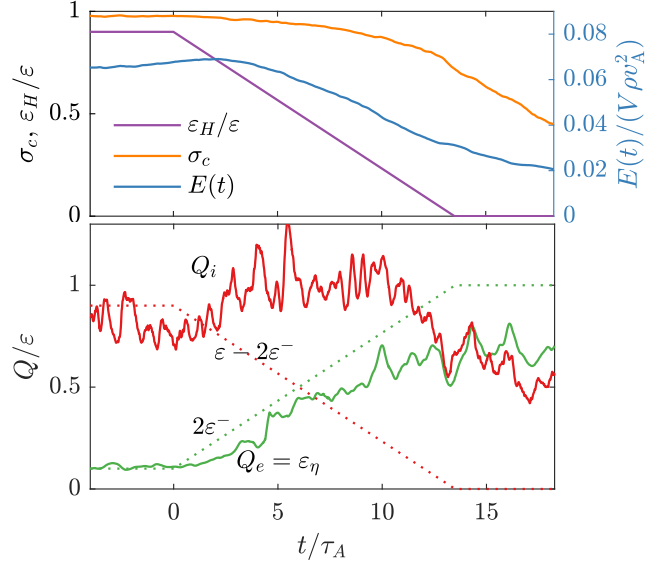
Figure 1. (*Top*) Time evolution of $\varepsilon_H/\varepsilon$ (purple), energy imbalance σ_c (orange), and total fluctuation energy per unit volume $E_{\perp}(t)$ (blue). (*Bottom*) Electron heating rate $Q_e = \varepsilon_{\eta}$ (green) and ion heating rate Q_i (red), with simple helicity-barrier expectations based on the forcing shown with dotted lines.

starts at $\sigma_c \approx 0.98$ for $t < 0$, then decreases as the system adjusts to the changing forcing ($\varepsilon_H/\varepsilon$). We halt the simulation once $\sigma_c \simeq 0.4$, a value similar to that in the solar wind around 1 au; as shown below, the heating properties have changed significantly by this point even though σ_c is still nonzero. The blue line shows the fluctuation energy density $E_{\perp} = \langle nm_i(|\boldsymbol{u}_{\perp}|^2 + |\boldsymbol{b}_{\perp}|^2) \rangle/2$, which decreases significantly over the simulation, as expected because the turbulence can dissipate more effectively at lower $\varepsilon_H/\varepsilon$.

The lower panel of Fig. 1 provides the measured heating rates, Q_i and $Q_e \equiv \varepsilon_{\eta}$ for ions and electrons, respectively. For most of the simulation, we see good agreement between ε_{η} (green line) and the helicity-barrier prediction $Q_e = 2\varepsilon^-$ (dotted-green line), aside from a delay of $\sim \tau_{\mathrm{A}}$ as the injected energy cascades towards smaller scales. The ion heating increases initially because the energy $E_{\perp}(t)$ decreases while the flux to hyper-resistive scales is fixed by the helicity barrier (the value of Q_i is unrealistically high because a slower evolution of $\varepsilon_H/\varepsilon$, and thus $E_{\perp}(t)$, implies that $Q_i = \varepsilon - Q_e - \partial_t E_{\perp} \approx \varepsilon_H - \partial_t E_{\perp}$ should more closely track ε_H). As $\varepsilon_H/\varepsilon$ nears zero ($t/\tau_{\mathrm{A}} \gtrsim 10$) and the helicity barrier erodes, the heating departs from $Q_e \approx 2\varepsilon^-$ and approaches that found in kinetic simulations of balanced turbulence at $\beta \approx 0.3$ (Kawazura et al. 2019; Cerri et al. 2021), in which ion heating via Landau damping and stochastic heating absorbs a portion of the energy flux before it reaches the smallest scales.
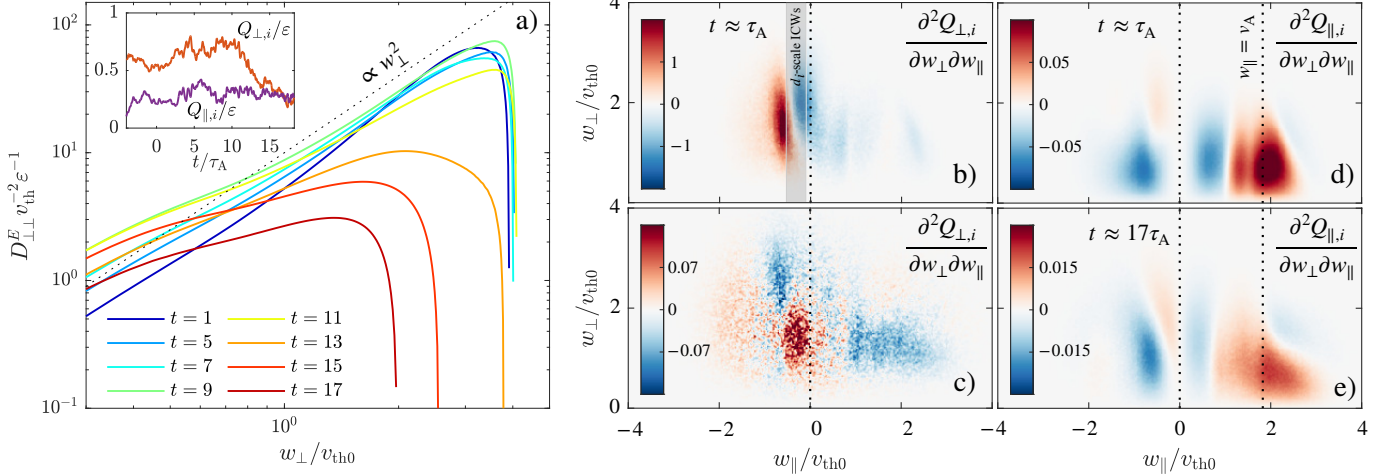
Figure 2. (*Left*) Time evolution of the perpendicular diffusion energy coefficient $D_{\perp\perp}^E$, showing the transition from the quasi-linear expectation $D_{\perp\perp}^E \propto w_\perp^2$ to a flatter profile around $t \gtrsim 11\tau_A$. The inset shows the normalized perpendicular (orange) and parallel (purple) ion heating rates, illustrating a sharp drop in $Q_{\perp,i}$ associated with the change in $D_{\perp\perp}^E$, while $Q_{\parallel,i}$ remains almost constant. (*Right*) Differential heating rates, $\partial^2 Q_{\perp,\parallel,i}/\partial w_\perp \partial w_\parallel$, computed from $\langle \boldsymbol{E}_{\perp,\parallel} \cdot \boldsymbol{w}_{\perp,\parallel} \rangle$. The $Q_\perp$ profile (panels b and c) exhibits resonant structure at early times (top); the shaded region shows $w_{\parallel\mathrm{res}}$ for oblique ICWs with $d_i^{-1} < k_\parallel < 2d_i^{-1}$, around where there is a sharp dropoff in wave power (Fig. 3). By late times it drops significantly and an ill-defined peak around $w_\perp \simeq v_{\mathrm{th}}$ appears, reminiscent of stochastic heating. The $Q_\parallel$ profile (panels d and e) maintains its structure, although spreads out modestly (accounting partially for its lower values).

The transition that causes the drop in ion heating is diagnosed in Fig. 2. We show the perpendicular energy-diffusion coefficient $D_{\perp\perp}^E$ (panel a), which is computed from the measured evolution of f_i via

$$D_{\perp\perp}^E = \left(\frac{\partial f_i}{\partial e_\perp}\right) \int_0^{e_\perp} \mathrm{d}e'_\perp \frac{\partial f_i(e'_\perp)}{\partial t}, \qquad (5)$$

where $e_\perp \equiv w_\perp^2/2$ and $f_i(e_\perp) = \int \mathrm{d}w_\parallel w_\perp f_i(w_\perp, w_\parallel)$. Equation (5) is taken directly from the $D_{\perp\perp}^E$ definition, $\partial f_i/\partial t = \partial/\partial e_\perp(D_{\perp\perp}^E \partial f_i/\partial e_\perp)$ (Vasquez et al. 2020), averaging over possible $w_\parallel$ variation and assuming that the heating is predominantly perpendicular, as appropriate for $t \lesssim 12\tau_A$ (Fig. 2a inset). For a spectrum of parallel waves, quasi-linear theory predicts $D_{\perp\perp}^E \propto w_\perp^2$, because the resonance condition and wave-polarization factors depend only on $w_\parallel$ (Kennel & Engelmann 1966). Although the wave spectrum here is more complex, involving a mix of oblique and parallel ICW modes (see below), this prediction is nonetheless well satisfied until $t \approx 11\tau_A$.[1] After this, $D_{\perp\perp}^E$ drops and flattens, causing a large drop in the perpendicular ion heating $Q_{\perp,i}$, even while the parallel heating $Q_{\parallel,i}$ remains almost constant (see inset). At later times, the form of $D_{\perp\perp}^E$ does not clearly indicate a particular heating mechanism, but is plausibly consistent with stochastic heating (Chandran

et al. 2010a); computing the $D_{\perp\perp}^E$ predicted for stochastic heating using the method of Cerri et al. (2021) gives a similar shape (not shown). As a complementary analysis, panels (b) and (c) display $\partial^2 Q_{\perp,i}/\partial w_\perp \partial w_\parallel$, computed directly from $\langle \boldsymbol{E}_\perp \cdot \boldsymbol{w}_\perp \rangle$ evaluated along particle trajectories (the so-called field-particle correlation technique; Klein & Howes 2016; Arzamasskiy et al. 2019). At early times a resonant feature is centered around the $w_\parallel$ that resonates with the smallest-(d_i)-scale oblique ICWs with significant power (the shaded region shows $w_{\parallel\mathrm{res}}$ for $d_i^{-1} \lesssim k_\parallel \lesssim 2d_i^{-1}$; see Fig. 3); at later times, the magnitude drops significantly into a diffuse peak around $w_\perp \simeq v_{\mathrm{th}}$, consistent with stochastic heating. In contrast, $\partial^2 Q_{\parallel,i}/\partial w_\perp \partial w_\parallel$ (panels d and e), maintains a form consistent with Landau damping of kinetic Alfvén waves (KAWs) throughout the simulation.

In Fig. 3 we provide evidence that the shut off in ion heating occurs because the turbulence amplitude decreases to the point where it can no longer drive quasi-linear heating by oblique ICWs. In the top panels, we show 2D spectra of $\delta B_\perp$ fluctuations, $\mathcal{E}_{B_\perp}(k_\perp, k_\parallel)$, which are computed by interpolating $k_\perp$-filtered fields onto the exact magnetic-field lines (S+22). Energy is concentrated at $k_\perp > k_\parallel$ (the turbulence) and in a bump at $k_\perp \ll k_\parallel \simeq 0.8d_i$ (parallel ICWs). Examining the time evolution from left to right, we see that the energy migrates to lower $k_\parallel$ with time (it moves downwards), with the dotted white lines indicating how this follows the critical-balance scaling $k_\parallel v_A = Ak_\perp z_{\mathrm{rms}}^+(k_\perp/k_{\perp 0})^{-1/3}$ (the coefficient $A = 2$ is chosen to align with the "peak" on the cone and is consistent

---

[1] The effect of obliquity is to flatten $D_{\perp\perp}^E$ at larger $w_\perp$, particularly for shorter-wavelength waves (Isenberg & Vasquez 2011). The highest-$k_\parallel$ waves here are mostly parallel propagating (Fig. 3) so these effects are likely minor.
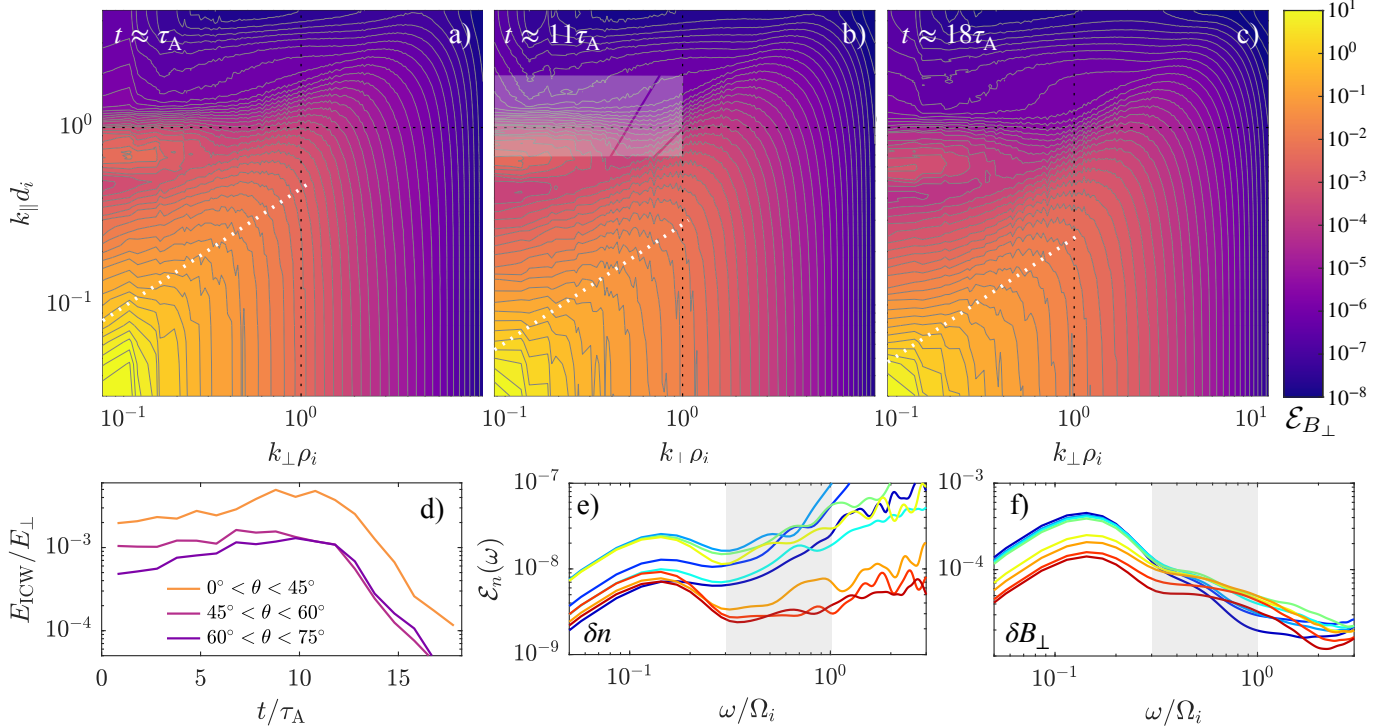
Figure 3. (a)–(c) 2D spectra of $\delta B_\perp$, $\mathcal{E}_{B_\perp}(k_\perp, k_\parallel)$, at $t \approx \tau_A$ (left), $t \approx 11\tau_A$ (around the time of the heating transition; middle), and $t \approx 18\tau_A$ (right). The dotted white lines show the critical-balance condition $k_\parallel v_A = 2k_\perp z_{\rm rms}^+ (k_\perp/k_{\perp 0})^{-1/3}$. (d) $E_{\rm ICW}$ for different ICW obliquities, which is the energy contained in the shaded regions of panel (b) (see text). (e)–(f) Frequency spectra at different times, using the same colors as Fig. 2a. A sharp drop in high-frequency δn fluctuations, taken as a signature of oblique ICW activity, matches the drop in $D_{\perp\perp}^E$. In contrast, $\delta B_\perp$ fluctuations, present in both parallel and oblique ICWs, drop less abruptly and at later times.

across time). A corollary is that larger-amplitude turbulence feeds more power into smaller-$k_\parallel$ oblique ICWs with smaller $w_{\parallel\rm res}$, driving more quasi-linear heating.

We quantify this effect in panel (d) by computing the energy of ICW fluctuations ($E_{\rm ICW}$), defined as those with $0.7 \leq k_\parallel d_i \leq 2$, as a function of wavevector obliquity $\theta = \tan^{-1}(k_\perp/k_z)$. The minimum wavenumber $k_\parallel d_i = 0.7$ is chosen to include waves for which $w_{\parallel\rm res} \sim v_{\rm th}$ (i.e., those that interact with the VDF core; Isenberg & Vasquez 2011), while the angle ranges capture quasi-parallel ($0 < \theta < 45°$), moderately oblique ($45° < \theta < 60°$), and highly oblique ($60° < \theta < 75°$) populations; these ranges are indicated by the shaded regions in panel (b). The energies of the oblique ICW populations start dropping rapidly around $t \approx 12\tau_A$. The coincidence of this sharp drop with the observed changes to $Q_\perp$ and $D_{\perp\perp}^E$ provides good evidence for oblique ICWs being the primary driver of heating (the slight increase in $E_{\rm ICW}$ for $t \lesssim 12\tau_A$, despite $E_\perp$ decreasing, is explained by the transition-range spectral drop moving to smaller scales; see below). The energy of parallel ICWs ($\theta \lesssim 45°$) follows a similar trend, but they are not driven directly by the turbulence, which has little power at $k_\parallel \gtrsim k_\perp$. Instead they arise because oblique-ICW quasi-linear heating causes f_i to increase

along the "resonance contours" of parallel ICWs (see below), thus emitting waves (causing instability; Kennel & Wong 1967; Chandran et al. 2010b). Their energy, which is driven and undamped during the oblique-ICW heating, builds up substantially for $t \lesssim 12\tau_A$, then decreases at later times as f_i changes shape and renders parallel ICWs stable and damped. Further evidence for this scenario is shown in panels (e) and (f), which show frequency spectra $\mathcal{E}(\omega)$ of the fluctuations in density δn (e) and $\delta B_\perp$ (f) at different times matching Fig. 2 (we highlight the ICW frequency range of interest, $0.3 \lesssim \omega/\Omega_i \lesssim 1$). While both parallel and oblique ICWs involve $\delta B_\perp$ fluctuations, only oblique modes involve δn. Indeed, we see a significant drop in $\mathcal{E}_{\delta n}$ at the same time as the drop in $Q_\perp$, while $\mathcal{E}_{\delta B_\perp}$ drops more smoothly and only for $t \gtrsim 13\tau_A$ (orange to red lines). The behavior of $\mathcal{E}_{\delta B_\perp}$ is consistent with the $0 < \theta \leq 45°$ $E_{\rm ICW}$ line in panel (d), which only drops below its initial value at $t \approx 13.5\tau_A$. An important consequence of this form of oblique-ICW heating is that it does not saturate when f_i becomes flat along the quasi-linear resonant contours, as would heating via parallel ICWs (Chandran et al. 2010b).

The effect of these dynamics on f_i is illustrated in Fig. 4, whose top panel superimposes isocontours of
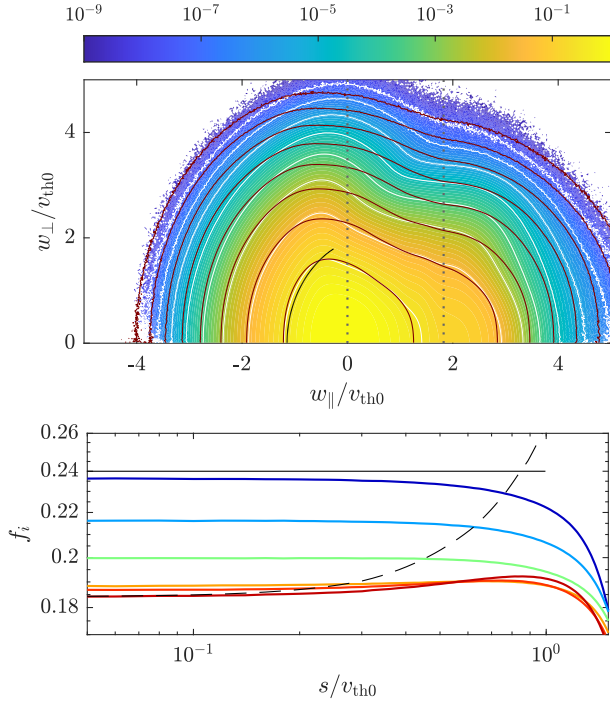
Figure 4. (*Top*) Contours of the ion VDF f_i at $t \approx 5\tau_A$ (white lines and colormap) and the $t \approx 18\tau_A$ (red lines). Dotted vertical lines highlight $w_\parallel = 0$ and $w_\parallel = v_A$. The red contour levels are chosen to emphasize changes in f_i and do not correspond to the white contours (see text). (*Bottom*) f_i versus distance s along the oblique-ICW resonant contour shown with the black line in the top panel ($s = 0$ at $w_\parallel = 0$). Colors are as in Fig. 2a. The thin-black line is flat ($\mathcal{G}[f_i] = 0$), while the dashed line shows an f_i that is independent of $w_\perp$ (as expected from stochastic heating).

$f_i(w_\perp, w_\parallel)$ at $t \approx 18\tau_A$ over $f_i(w_\perp, w_\parallel)$ at $t \approx 5\tau_A$. The quasi-linear heating scatters particles to make f_i constant along the "resonant contours," $\mathcal{G}[f_i] = 0$, where $\mathcal{G} \equiv (1 - k_\parallel w_\parallel / \omega) \partial / \partial w_\perp + (k_\parallel w_\perp / \omega) \partial / \partial w_\parallel$ is the quasi-linear scattering operator. Because the heating is driven by oblique ICWs but excites parallel ICWs, for $t \lesssim 11\tau_A$, f_i decreases along the oblique-ICW contours (with $\omega = k_\parallel v_A / \sqrt{1 + k_\parallel^2 d_i^2}$) and increases along the parallel-ICW contours (with $\omega = k_\parallel v_A \sqrt{1 - \omega/\Omega_i}$; Chandran et al. 2010b; Isenberg & Vasquez 2011). Its evolution towards a flatter core at $t \gtrsim 11\tau_A$ is hard to discern on $f_i(w_\perp, w_\parallel)$, so in the lower panel we plot f_i along an oblique-ICW resonant contour (thin black line). It changes from decreasing slightly to increasing along the contour, with the latter a signature of $f_i(w_\perp, w_\parallel)$ becoming flatter in $w_\perp$, likely due to stochastic heating (a $w_\perp$-independent f_i is shown with the dashed line; Klein & Chandran 2016; Cerri et al. 2021). Various other modifications to f_i over the simulation are clear in the top panel, including the smoothing of the sharp "ridge" bor-
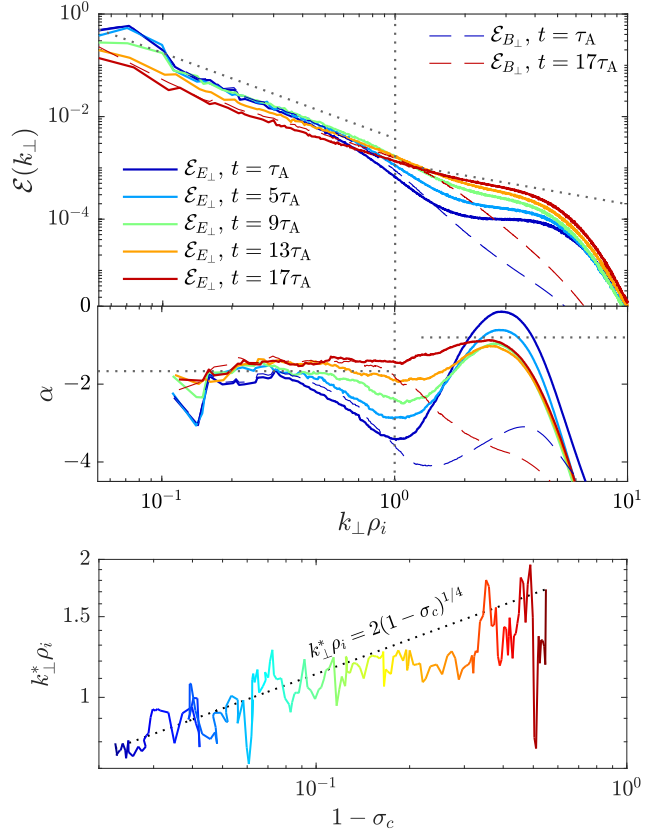
Figure 5. (*Top*) Perpendicular spectra of the electric field ($\mathcal{E}_{E_\perp}$; solid lines) and magnetic field ($\mathcal{E}_{B_\perp}$; solid lines) at a selection of times. The sub-panel illustrates the local spectral slopes α; the dotted lines indicate $k_\perp \rho_i = 1$ and the representative power laws $k_\perp^{-5/3}$ and $k_\perp^{-0.8}$. (*Bottom*) Evolution of the break scale $k_\perp^*$ with imbalance $1 - \sigma_c$, with the line color indicating the time as in the top panel. The dotted line shows the empirical scaling $k_\perp^* \rho_i = 2(1 - \sigma_c)^{1/4}$, which provides a good fit to the simulation until $t \approx 11\tau_A$.

dering the quasi-linearly heated region of phase space at $w_\parallel / v_{\text{th0}} \approx -0.5$, and the flattening of $f_i(w_\perp)$ at $w_\parallel > 0$.

Another feature of f_i is the strong parallel plateau, or beam, which results from the Landau damping of $k_\perp \gg k_\parallel$ fluctuations at $k_\perp \rho_i \lesssim 1$ (see also S+22; Li et al. 2010). Such fluctuations, which lie in the $k_\perp$ range between Alfvén waves and KAWs, propagate with phase speed $> v_A$ (Howes et al. 2006), growing a modestly super-Alfvénic plateau in f_i. As the turbulence becomes balanced, such fluctuations would likely flatten f_i at $w_\parallel \approx -v_A$ also (see figure 7 of Arzamasskiy et al. 2019), but this feature is not yet observable. The total parallel heating $Q_{\parallel,i}$, which captures this beam formation, remains almost constant throughout the full simulation (Fig. 2a inset). This suggests the $k_\perp \rho_i \sim 1$ Alfvénic fluctuations are Landau damping some fixed portion of their energy before dissipating into oblique

ICWs (at earlier times) or KAW turbulence (at later times). A corollary is that there is no fundamental difference between the beam formation and standard resonant parallel heating, aside from the fluctuations' imbalance.

Finally, Fig. 5 shows the evolution of the perpendicular spectra $\mathcal{E}(k_\perp)$ of $\boldsymbol{E}_\perp$ and $\boldsymbol{B}_\perp$. The flatter sub-ρ_i range in the former helps to highlight the double-kinked "transition-range" power law; for $k_\perp \rho_i \lesssim 1.5$, including in the transition range, $\mathcal{E}_{E_\perp} \approx \mathcal{E}_{B_\perp}$. As the turbulence becomes balanced, the spectral break smoothly moves towards smaller scales, creating a less pronounced transition range that is narrower in $k_\perp$ and less steep, close to $\mathcal{E}_{E_\perp} \sim k_\perp^{-0.8}$. At late times, $\delta B_\perp$ is resistively damped by the larger resistivity and the magnetic spectrum does not exhibit a clear $\sim k_\perp^{-2.8}$ kinetic range.

The lower panel of Fig. 5 provides the evolution of the break scale $k_\perp^*$, obtained by fitting a broken power-law to $\mathcal{E}_{B_\perp}(k_\perp)$.[2] We find a clear power-law dependence on the energy imbalance, $k_\perp^* \rho_i \propto (1 - \sigma_c)^{1/4} \sim (z_{\mathrm{rms}}^- / z_{\mathrm{rms}}^+)^{1/2}$, for $\sigma_c \gtrsim 0.8$ ($t \lesssim 12\tau_{\mathrm{A}}$) when the barrier is active ($\varepsilon_H / \varepsilon \gtrsim 0$). Although this scaling remains unexplained theoretically, it matches the results of low-β gyrokinetic simulations for various choices of $\varepsilon_H / \varepsilon$ (Meyrand et al. 2021, figure 7), suggesting it is a robust consequence of the helicity barrier and independent of the energy-dissipation mechanism (gyrokinetics is ignorant of ICW kinetic physics). This $k_\perp^*$ scaling can also be used to understand the evolution of $Q_{\perp,i}$ by estimating the minimum accessible parallel scale as $k_{\parallel,\mathrm{max}} v_{\mathrm{A}} \sim k_\perp^* z_{\mathrm{rms}}^+ (k_\perp^*/k_{\perp 0})^{-1/3}$, then taking $k_{\parallel,\mathrm{max}} d_i$ as a proxy for the power injected into oblique ICWs, and therefore $Q_{\perp,i}$ (i.e., $Q_{\perp,i}$ is some function of $k_{\parallel,\mathrm{max}} d_i$). Taking $k_\perp^* \rho_i \propto (z_{\mathrm{rms}}^-/z_{\mathrm{rms}}^+)^{1/2}$ gives $k_{\parallel,\mathrm{max}} d_i \propto \beta^{-1/2} (k_{\perp 0} \rho_i)^{1/3} (z_{\mathrm{rms}}^+)^{2/3} (z_{\mathrm{rms}}^-)^{1/3} / v_{\mathrm{A}}$, the time evolution of which correlates very well with $Q_{\perp,i}$ (including during pre-saturated phase of S+22), increasing until $t \approx 3\tau_{\mathrm{A}}$ and then remaining approximately constant for $t \lesssim 11\tau_{\mathrm{A}}$ even though $z_{\mathrm{rms}}^\pm$ change substantially (cf. Fig. 1).

4. DISCUSSION

A complete theory for the helicity barrier would be able to predict the parameters ($\varepsilon_H / \varepsilon$, β, etc.) at which it is operative. Low-β gyrokinetics states only that the barrier occurs unless the generalized helicity can be destroyed at least as fast as $\sim \varepsilon_H$ before $k_\perp \rho_i \sim 1$ scales are reached (Meyrand et al. 2021). Although generalized helicity is not a true invariant of hybrid kinetics, we can

infer from our simulation, based on the agreement between Q_e and $2\varepsilon^-$ (Fig. 1) and the continuous evolution of the transition-range spectrum (Fig. 5) for $t \lesssim 10\tau_{\mathrm{A}}$, that the critical $\varepsilon_H / \varepsilon$ at $\beta \approx 0.3$ is ≈ 0.2. The changes that occur once $\varepsilon_H / \varepsilon \lesssim 0.2$ also coincide with the sharp drop in $Q_{\perp,i}$ (Fig. 2), suggesting that breaking the helicity barrier curtails ion heating. These results highlight the surprising robustness of the helicity barrier in the face of the additional complexities of a true kinetic system. However, $\varepsilon_H / \varepsilon$ decreases unrealistically fast in our simulation; understanding how the barrier evolves when $\varepsilon_H / \varepsilon$ changes on timescales comparable to the turbulent decay time should be a priority for future work.

Our results provide a helpful roadmap for understanding the radially dependent interplay between turbulence, heating, and instabilities in the $\beta \lesssim 1$ solar wind. At smaller R and in faster streams, which have higher observed imbalance, we predict strong perpendicular ion heating via quasi-linear resonance, continual emission of parallel ICWs, a steep and wide ion-Larmor-scale transition range, proton beam formation, and little electron heating. At larger R and in slower streams, which have lower imbalance ($\sigma_c \lesssim 0.8$ in our simulation), electron heating dominates, parallel ICWs are absorbed/damped, there is no transition-range spectrum, and sharp features in the VDF are smoothed out. These correlations and features match those measured in the low-β solar wind by *in situ* spacecraft (e.g., Marsch 2006; Bruno et al. 2014; Zhao et al. 2021).

Under the assumption that, far from the Sun, faster wind is heated more than slower wind (Hansteen & Leer 1995; Totten et al. 1995; Halekas et al. 2023), our results explain qualitatively various interesting properties of observed temperature profiles. Close to the Sun, proton and minor-ion temperatures correlate positively with wind speed (Burlaga & Ogilvie 1973), while the electron temperature is negatively correlated (Marsch et al. 1989); this is natural if the highly imbalanced turbulence of faster streams has low Q_e/Q_i (Shi et al. 2023). At larger distances (~ 1 au), the electron-temperature correlation flips to positive for $U \lesssim 500$ km s^{-1} (Shi et al. 2023), as would occur if Q_e/Q_i increased to $\gtrsim 1$ as the turbulence becomes balanced at larger radii. More directly, Abraham et al. (2022) measure $Q_e \propto R^{-2}$ for $R \lesssim 0.3$ au, followed by a rapid drop in Q_e at larger R. This profile, $Q_e \propto R^{-2}$, is much flatter than the "standard" total-heating profile $Q \propto R^{-4}$ (e.g., Totten et al. 1995)—a natural explanation is that $Q = Q_i + Q_e$ is steeper than Q_e, because Q_e/Q_i increases as $\varepsilon_H / \varepsilon$ decreases with R. Then, once $\varepsilon_H / \varepsilon \ll 1$ (around $R \simeq 0.3$ in this scenario), Q_e/Q_i saturates and Q_e drops rapidly.

Together, these observations suggest that imbalanced turbulence and the helicity barrier are actively shaping global coronal and solar-wind dynamics. More generally, they highlight the crucial role of imbalance in controlling collisionless plasma thermodynamics.

---

[2] The functional form of the fit is $\mathcal{E}_{\mathrm{fit}} = [(k_\perp/k_\perp^*)^{n\alpha_1} + (k_\perp/k_\perp^*)^{n\alpha_2}]^{-1/n}$, where α_1 (α_2) is the power-law index for $k_\perp < k_\perp^*$ ($k_\perp > k_\perp^*$), and n controls the break's sharpness; we fit $\mathcal{E}_{B_\perp}(k_\perp)$ in the range $0.14 < k_\perp \rho_i < 2$. The measured proportionality between $k_\perp^* \rho_i$ and $(1-\sigma_c)^{1/4}$ varies with fitting choices, but the power-law exponent $(1/4)$ is robust.

REFERENCES

Abraham, J. B., Verscharen, D., Wicks, R. T., et al. 2022, Astrophys. J., 941, 145, doi: 10.3847/1538-4357/ac9fd8

Arzamasskiy, L., Kunz, M. W., Chandran, B. D. G., & Quataert, E. 2019, Astrophys. J., 879, 53, doi: 10.3847/1538-4357/ab20cc

Arzamasskiy, L., Kunz, M. W., Squire, J., Quataert, E., & Schekochihin, A. A. 2023, Phys. Rev. X, 13, 021014, doi: 10.1103/PhysRevX.13.021014

Bowen, T. A., Chandran, B. D. G., Squire, J., et al. 2022, Phys. Rev. Lett., 129, 165101, doi: 10.1103/PhysRevLett.129.165101

Bowen, T. A., Bale, S. D., Chandran, B. D. G., et al. 2023, arXiv:2306.04881, doi: 10.48550/arXiv.2306.04881

Bruno, R., & Carbone, V. 2013, Living Rev. Solar Phys., 10, 2, doi: 10.12942/lrsp-2013-2

Bruno, R., Trenchi, L., & Telloni, D. 2014, Astrophys. J. Lett., 793, L15, doi: 10.1088/2041-8205/793/1/L15

Burlaga, L. F., & Ogilvie, K. W. 1973, J. Geophys. Res., 78, 2028, doi: 10.1029/JA078i013p02028

Cerri, S. S., Arzamasskiy, L., & Kunz, M. W. 2021, Astrophys. J., 916, 120, doi: 10.3847/1538-4357/abfbde

Chandran, B. D. G., Li, B., Rogers, B. N., Quataert, E., & Germaschewski, K. 2010a, Astrophys. J., 720, 503, doi: 10.1088/0004-637X/720/1/503

Chandran, B. D. G., Pongkitiwanichakul, P., Isenberg, P. A., et al. 2010b, Astrophys. J., 722, 710, doi: 10.1088/0004-637X/722/1/710

Chen, C. H. K., Matteini, L., Schekochihin, A. A., et al. 2016, Astrophys. J., 825, 1, doi: 10.3847/2041-8205/825/2/l26

D'Amicis, R., Alielden, K., Perrone, D., et al. 2021, Astron. Astro., 654, A111, doi: 10.1051/0004-6361/202140600

Dobrowolny, M., Mangeney, A., & Veltri, P. 1980, Phys. Rev. Lett., 45, 144, doi: 10.1103/PhysRevLett.45.144

Duan, D., He, J., Bowen, T. A., et al. 2021, Astrophys. J. Lett., 915, L8, doi: 10.3847/2041-8213/ac07ac

Halekas, J. S., Bale, S. D., Berthomier, M., et al. 2023, arXiv:2305.13424, doi: 10.48550/arXiv.2305.13424

Hansteen, V. H., & Leer, E. 1995, J. Geophys. Res., 100, 21577, doi: 10.1029/95JA02300

Horbury, T. S., Wicks, R. T., & Chen, C. H. K. 2012, Space Sci. Rev., 172, 325, doi: 10.1007/s11214-011-9821-9

Howes, G. G., Cowley, S. C., Dorland, W., et al. 2006, Astrophys. J., 651, 590, doi: 10.1086/506172

Isenberg, P. A., & Vasquez, B. J. 2011, Astrophys. J., 731, 88, doi: 10.1088/0004-637X/731/2/88

Kawazura, Y., Barnes, M., & Schekochihin, A. A. 2019, Proc. Nat. Acad. Sci., 116, 771, doi: 10.1073/pnas.1812491116

Kennel, C. F., & Engelmann, F. 1966, Phys. Fluids, 9, 2377, doi: 10.1063/1.1761629

Kennel, C. F., & Wong, H. V. 1967, J. Plasma Phys., 1, 75, doi: 10.1017/S002237780000310X

Klein, K. G., & Chandran, B. D. G. 2016, Astrophys. J., 820, 47, doi: 10.3847/0004-637X/820/1/47

Klein, K. G., & Howes, G. G. 2016, Astrophys. J. Lett., 826, L30, doi: 10.3847/2041-8205/826/2/L30

Kunz, M. W., Stone, J. M., & Bai, X.-N. 2014, J. Comp. Phys., 259, 154, doi: 10.1016/j.jcp.2013.11.035

Li, X., Habbal, S. R., Hollweg, J. V., & Esser, R. 1999, J. Geophys. Res., 104, 2521, doi: 10.1029/1998JA900126

Li, X., Lu, Q., Chen, Y., Li, B., & Xia, L. 2010, Astrophys. J. Lett., 719, L190, doi: 10.1088/2041-8205/719/2/L190

Marsch, E. 2006, Living Rev. Solar Phys., 3, 1, doi: 10.12942/lrsp-2006-1

Marsch, E., Pilipp, W. G., Thieme, K. M., & Rosenbauer, H. 1989, J. Geophys. Res., 94, 6893, doi: 10.1029/JA094iA06p06893

Meyrand, R., Squire, J., Mallet, A., & Chandran, B. D. G. 2023, arXiv:2308.10389, doi: 10.48550/arXiv.2308.10389

Meyrand, R., Squire, J., Schekochihin, A. A., & Dorland, W. 2021, J. Plasma Phys., 87, 535870301, doi: 10.1017/S0022377821000489

Parker, E. N. 1965, Space Sci. Rev., 4, 666, doi: 10.1007/BF00216273

Roberts, D. A., Goldstein, M. L., Klein, L. W., & Matthaeus, W. H. 1987, J. Geophys. Res., 92, 12023, doi: 10.1029/JA092iA11p12023

Schekochihin, A. A. 2022, J. Plasma Phys., 88, 155880501, doi: 10.1017/S0022377822000721

Shi, C., Velli, M., Lionello, R., et al. 2023, Astrophys. J., 944, 82, doi: 10.3847/1538-4357/acb341

Squire, J., Meyrand, R., Kunz, M. W., et al. 2022, Nature Astron., 6, 715, doi: 10.1038/s41550-022-01624-z

Totten, T. L., Freeman, J. W., & Arya, S. 1995, J. Geophys. Res., 100, 13, doi: 10.1029/94JA02420

Vasquez, B. J., Isenberg, P. A., & Markovskii, S. A. 2020, Astrophys. J., 893, 71, doi: 10.3847/1538-4357/ab7e2b

Zhao, G. Q., Lin, Y., Wang, X. Y., et al. 2021, Astrophys. J., 906, 123, doi: 10.3847/1538-4357/abca3b